J Appl Physiol 103: 484–493, 2007.
First published April 19, 2007; doi:10.1152/japplphysiol.00315.2006.

A new class of biophysical models for predicting the probability of decompression sickness in scuba diving

Saul Goldman

Department of Chemistry and Guelph-Waterloo Physics Institute, University of Guelph, Guelph, Ontario, Canada

Submitted 14 March 2006; accepted in final form 16 April 2007

Goldman S. A new class of biophysical models for predicting the probability of decompression sickness in scuba diving. *J Appl Physiol* 103: 484–493, 2007. First published April 19, 2007; doi:10.1152/japplphysiol.00315.2006.—Interconnected compartmental models have been used for decades in physiology and medicine to account for the observed multi-exponential washout kinetics of a variety of solutes (including inert gases) both from single tissues and from the body as a whole. They are used here as the basis for a new class of biophysical probabilistic decompression models. These models are characterized by a relatively well-perfused, risk-bearing, central compartment and one or two non-risk-bearing, relatively poorly perfused, peripheral compartment(s). The peripheral compartments affect risk indirectly by diffusive exchange of dissolved inert gas with the central compartment. On the basis of the accuracy of their respective predictions beyond the calibration regime, the three-compartment interconnected models were found to be significantly better than the two-compartment interconnected models. The former, on the basis of a number of criteria, was also better than a two-compartment parallel model used for comparative purposes. In these latter comparisons, the models all had the same number of fitted parameters (four), were based on linear kinetics, had the same risk function, and were calibrated against the same dataset. The interconnected models predict that inert gas washout during decompression is relatively fast, initially, but slows rapidly with time compared with the more uniform washout rate predicted by an independent parallel compartment model. If empirically verified, this may have important implications for diving practice.

compartmental modeling; perfusion-diffusion models; multi-exponential exchange kinetics

SCUBA DIVING WITH AIR AS the breathing mixture, involves breathing compressed air. The compressed air is provided to the diver (through a "demand regulator") at ambient pressures. Because of the hydrostatic pressure of water, these ambient pressures will exceed the surface pressure. Consequently, during a dive, more nitrogen will be dissolved in blood and body tissues than is normally dissolved at surface pressures. A diver surfacing rapidly from a dive may have a considerable excess of dissolved nitrogen remaining in the blood and tissues. If the excess is large enough, some of the dissolved nitrogen will come out of solution in the form of bubbles which, if sufficiently extensive, can lead to "decompression sickness" (DCS). Severe forms of DCS can include paralysis or death. Therefore, the rate of the ascent, and/or the depth vs. time profile for the ascent, must be appropriately controlled.

Decompression models are highly simplified biophysical representations of the body and those regions or tissues of the body that are relevant to the development of DCS. These models are created in an attempt to capture and mimic the most salient factors that lead to DCS. They can be used to predict the probability of developing DCS [*P*(DCS)] for any dive and to prescribe ascent procedures that would constrain *P*(DCS) for a particular dive to an acceptable level.

This article describes the properties of probabilistic decompression models in which both perfusion and inter-tissue diffusion of dissolved inert gas influence *P*(DCS). The reason for including inter-tissue diffusion is that an accumulated body of empirical work has shown that inert gas blood-tissue exchanges, for a variety of gases and tissues, are best accounted for by models that involve a mix of perfusion and external diffusion-driven processes. These external processes include arterio-venous countercurrent exchange (5, 15), diffusion between unequally perfused tissues (4, 6, 15), and combinations of such effects (7). Superimposing external diffusion-driven processes onto an otherwise perfusion-limited compartment changes the wash-in/washout kinetics of the compartment from mono- to multi-exponential. This means the tissue-arterial gas concentration or pressure differences now decay as sums of exponentials rather than as single exponentials.

Originating with Haldane (2), a parallel network of independent, perfusion-limited compartments, of the kind illustrated in Fig. 1*A*, has been the mainstay of decompression modeling for about a century. A debate concerning whether such a model can adequately represent gas washout data, seems to have started some sixty years ago between Kety (17), on the one hand, and Morales and Smith (25–27, 31, 32), on the other. Morales and Smith proposed that a model with both perfusion and external diffusion, specifically, their "competitive parallel arrangement," was a more appropriate basis for representing the kinetics of gas washout from most tissues of the body than was either a series arrangement or an arrangement of independent, parallel, perfusion-limited compartments (26). Kety criticized the Morales and Smith model as unnecessarily complicated. He maintained that multi-exponential washout from a tissue could be adequately represented by the simpler parallel arrangement of independent perfusion-limited compartments if sufficient numbers of such compartments were included in the model of the tissue (17).

Subsequently, Novotny et al. (29) carried out a study that directly tested Kety's assertion. This group attempted to fit the kinetics of ^{133}Xe washout from dog calf muscle, modeled as an independent parallel network of more than 100 perfusion-limited compartments. The study found the model's predictions of key physiological functions to be very inaccurate. For example, the observed mean tissue transit time of ^{133}Xe was

Address for reprint requests and other correspondence: S. Goldman, Dept. of Chemistry and the Guelph-Waterloo Physics Institute, Univ. of Guelph, Guelph, Ontario, Canada N1G 2W1 (e-mail: goldman@chembio.uoguelph.ca).

The costs of publication of this article were defrayed in part by the payment of page charges. The article must therefore be hereby marked "*advertisement*" in accordance with 18 U.S.C. Section 1734 solely to indicate this fact.

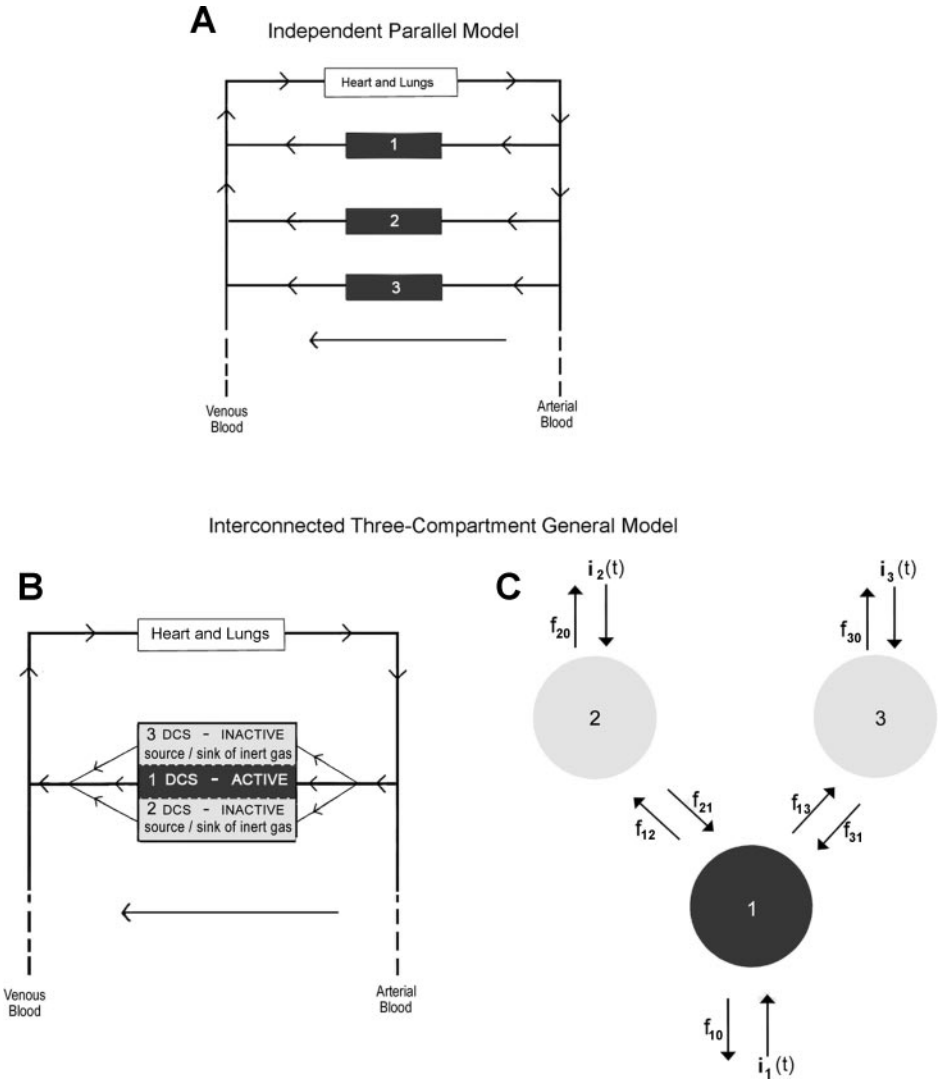

Fig. 1. *A*: the independent parallel compartment model in which each compartment bears risk. *B*: the three-compartment general model (3CG) in which the central compartment alone bears risk. *C*: the compartmental representation of the 3CG model with rate constants f_{ij} for dissolved N_2 transfer and input functions $i_j(t)$. DCS, decompression sickness.

6.7 times longer than the value predicted by Kety's model for this system.

More recently, Doolette et al. found additional inconsistencies associated with the application of parallel perfusion-limited models in sheep (5–7). These workers found that the models, which involved a mix of perfusion-limited and external diffusion-driven processes, provided improved agreement with their data.

In addition to these studies, the general idea that DCS-prone tissue is unlikely to be isolated from less susceptible tissues and may be indirectly affected by them has been around for some time. For example, 17 years ago, Vann pointed out the possibility that unsusceptible tissue (such as lipid) may act as a reservoir of dissolved inert gas relative to contiguous, more susceptible tissue and may thereby, indirectly, affect DCS risk by diffusive exchange of inert gas with the susceptible tissue (38).

In view of the above, it seems timely to investigate the properties of decompression models consisting of interconnected compartments of differing susceptibilities to DCS and that involve a mix of perfusion and external diffusion. Before proceeding, however, the preexisting work on interconnected decompression models and compartmental, multi-exponential kinetics is briefly outlined.

The "Kidd-Stubbs" model (18, 28, 36) is an interconnected, series, four-compartment decompression model that is similar to the models developed here in one important respect: the compartments, because they are interconnected, each follow multi-exponential kinetics. It differs from the models developed here in two fundamental ways. First, the Kidd-Stubbs model includes a quadratic contribution to the kinetics, whereas, here, to render the rate equations analytically solvable, linear kinetics is assumed. Second, in the interconnected models studied here, only the relatively well perfused central compartment contributes explicitly to the risk, whereas, in the Kidd-Stubbs model, all the compartments are potentially risk-bearing. It should be noted, however, that an important derivative of the Kidd-Stubbs model [the DCIEM 1983 model (28)] has risk associated with only the first two (outermost) compartments of the series. As with the interconnected models studied here, the non-risk-bearing compartments in this derivative model influence risk indirectly.

In addition, earlier exploratory calculations on compartments that involve two-exponential kinetics have been carried out (39, 41). It was noted in Ref. 41 that the relatively slow washout of nitrogen found for the two-exponential compartment studied reflected the double exponential residence time

function used to describe gas-exchange experiments on dogs (39, 41).

To ensure continuity and accessibility, most of the technical and mathematical details are given separately in the three appendices that are provided online at the *Journal of Applied Physiology* website. The underlying ideas and results should be clear from the main body of the article alone.

Models. The probabilistic approach to decompression theory, developed by Weathersby and his coworkers (Refs. 34, 36, 40, 42, 43, and references therein), was used here for several reasons. It is more realistic than the earlier deterministic approach, and the models used with it are relatively simple. Such models can be formulated with a minimum of adjustable parameters, and they are structured in a way that is well suited to the present purpose. They consist of two separate and distinct components: one describing how excess gas is distributed over the compartments; the other a risk function. This makes it possible, by comparing different gas-distribution models that share a common risk function, to determine how the choice for the gas distribution model alone influences the overall properties of the model.

The type of interconnected gas distribution models that were studied are illustrated in Fig. 1, *B* and *C*. Biophysical models of this kind (but without a risk-bearing compartment) that include mammillary, catenary, and other interconnected models have been used in physiology and medicine for decades (16). They are used to account for the empirically observed multi-exponential washout kinetics for a variety of solutes, both from individual tissues and from the body as a whole (16, chapter 17). Their defining characteristics are that their "compartments," defined simply as macroscopic subsystems, are "well mixed" (i.e., homogeneous) and that they interact by exchanging material with each other. For this application, a method of determining DCS risk is needed as well.

As discussed in the introduction, models that involve a mix of perfusion and intercompartmental diffusion and whose compartments, as a consequence, display multi-exponential kinetics seem best at accounting for observed inert gas blood-tissue washout curves. A central premise of this work is that DCS-prone tissue is not exceptional in this regard. It is also generally accepted that not all regions/tissues of the body are equally susceptible to decompression injury (12, 38). Unlike what was tacitly, and almost invariably, done in the past [the sole exception being the DCIEM 1983 model (28)], it is here not assumed that unsusceptible tissue is irrelevant to the prediction of DCS risk. The model shown in Fig. 1, *B* and *C*, was constructed with these factors in mind. As shown, the central compartment alone is assumed to bear risk, so it alone is associated with a risk function. The washout kinetics of this compartment, which will directly influence the risk function, will, like that of the other compartments, be multi-exponential and will be influenced both by perfusion and by intercompartmental diffusion. The peripheral compartments represent contiguous regions that are relatively unsusceptible to decompression injury. They exchange inert gas by diffusion with the central compartment and affect risk indirectly by acting as either sources or sinks of dissolved inert gas for the central compartment. Intercompartmental diffusion between the central and peripheral compartments is taken to arise from unequal perfusion of the contiguous compartments. Specifically, the central compartment is assumed to be well perfused[1] relative to the peripheral compartments.

Four interconnected compartmental models will be considered: two with two compartments apiece and two with three compartments apiece. The two- and three-compartment models will be characterized by two- and three-exponential compartmental kinetics, respectively (16, chapter 2). Figure 1, *B* and *C*, illustrates what will be called the three-compartment general model (3CG). As shown, all the compartments are here perfused by the circulatory system, but the central compartment is taken to be better perfused than the peripheral compartments. The so-called three-compartment mammillary model (3CM) is obtained by severing the connections (inputs and outputs) of *compartments 2* and *3* with the circulatory system (16, chapter 2). Thus, in the 3CM model, the peripheral compartments are totally unperfused, have no output to the circulatory system, and exchange nitrogen by diffusion only with the central compartment, which retains its connections to the circulatory system. The two-compartment general model (2CG) is obtained by removing one of the peripheral compartments (e.g., *compartment 3*) from the 3CG model, and the two-compartment mammillary model (2CM) is then obtained from this 2CG model by severing the connections of *compartment 2* with the circulatory system (see APPENDIX A, available online at the *Journal of Applied Physiology* website, for details).

Because of the computational requirements associated with this application, linear kinetics is here assumed. Under linear kinetics, wherein transfer rates are proportional to the first power of the relevant pressure differences, the rate equations can be solved analytically, i.e., both exactly and very rapidly. This is essential for keeping the calculations simple and the computer time requirements low (see APPENDICES A and B, available online at the *Journal of Applied Physiology* website).

This work deals with the influence of a decompression model's compartmental structure on its properties. The issues of how best to define the risk function, or what its basis ought to be, are not addressed. The approach taken was to use a simple risk function of exactly the same functional form for all the models. This was done to ensure that comparisons among the models would reflect differences due only to the form assumed for the gas-distribution part of the model.

The risk function used was of the dissolved gas (or single phase) type, developed by Weathersby and coworkers (34, 36). It was

$$r_i(t) = \frac{c_i[p_i(t) - (P_0(t) + B)]}{P_0(t)} \qquad (1)$$

where $B \equiv (P_{th} - P_{fvg})$, the subscript i designates the compartment number, $r_i(t)$ is the risk per unit time, c_i is a proportionality constant, $p_i(t)$ is the Henry's law-based dissolved inert

[1] "Well-perfused" here implies a relatively large perfusional rate constant (or fractional transfer coefficient) f_{i0}. These constants differ from "flow rate per unit volume," a commonly used measure of perfusion, by a factor involving the gas partition coefficient. As used here, "a relatively well perfused central compartment" implies the following relations between the perfusion-based f_{i0}s: $f_{10} >> f_{20}$; $f_{10} >> f_{30}$. If the compartments were uniformly perfused, in the sense that $f_{10} = f_{20} = f_{30}$, the chemical potential or, equivalently, the Henry's law-based partial pressure of nitrogen would be the same in all the compartments (11, 21). It would rise and fall exactly in unison in all the compartments, and no driving force for intercompartment diffusion would exist.

gas partial pressure (11, 21), $P_0(t)$ is the total ambient hydrostatic pressure, and P_{th} and P_{fvg} are, respectively, the "threshold" and "fixed venous gas" pressures (below, and APPENDIX C, available online at the *Journal of Applied Physiology* website). For all the interconnected compartmental models (2CM, 2CG, 3CM, and 3CG) i was 1. For the two-compartment, independent, parallel model used for comparison (2CP), i was 1 and 2, since here each compartment carries risk.

The term B carries contributions to $r_i(t)$ from effects other than those due to the relative excess nitrogen partial pressure: $[p_i(t) - P_0(t)]/P_0(t)$. P_{fvg}, which accounts approximately for the influence of the venous gases $H_2O(g)$, $CO_2(g)$, and $O_2(g)$, increases the risk by adding the sum of the partial pressures of these gases to that of $N_2(g)$. P_{th}, on the other hand, provides an approximate contribution to risk reduction that arises from the existence of a threshold depth (d_{th}). Here, d_{th} refers to the deepest depth from which rapid decompression to $P_0 = 1$ atm will never cause DCS, even when the time spent at that depth is sufficient to ensure saturation; i.e., 1 day or more. It was here found to be 11.7 fsw (APPENDIX C), where fsw represents "feet of sea water." The values used for P_{fvg}, P_{th}, and B were 0.192 atm, 0.213 atm, and 0.021 atm, respectively. The value of P_{fvg} was taken from Ref. 34, and P_{th} was determined from d_{th} as described in APPENDIX C. The value 0.021 atm for B was used in the $r_i(t)$ expressions of all five models. In addition, as described in APPENDIX C, a different value of B, stemming from a different choice made for d_{th} was used in supplementary trial calculations. These calculations were carried out to assess the sensitivity of the interconnected models with respect to the value used for d_{th} or B. The main result was that the qualitative properties of the interconnected models do not depend on a specific value of d_{th} or B.

METHODS

Calibrations. This is an initial demonstration paper. Its purpose is not to present new models ready for application. Rather, its purpose is to compare the properties and the potential usefulness of models with the structure illustrated in Fig. 1*B*, against those with the structure illustrated in Fig. 1*A*. This bears directly on how the dataset to be used for the calibrations was chosen.

An important test of the potential usefulness of a model is its "robustness." A robust model is one that is relatively insensitive to the regime in which it is applied. For example, if *model x*, which is calibrated against a low-risk square profile dataset, is subsequently found to accurately predict the *P*(DCS) values of a high-risk square profile dataset, then *model x* demonstrates some robustness. The robustness stems from the applicability of same parameter values of *model x* in the two different regimes. Clearly, this is a useful property. If this same *model x* also accurately predicts the *P*(DCS) values of a very low-risk multilevel profile dataset, then *model x* is that much more robust and useful. Although robustness here is suggestive of a model's capturing the salient features of the underlying physiology, this is not necessarily the case and, in any event, is irrelevant to the present purpose.

We therefore require both a dataset consisting of profiles of a particular kind (for purposes of calibration), and additional data that can be used to check the quality of the calibrated model's extrapolations. If the extrapolations are to be meaningful, the differences between the two sets of data must be both well defined and significant. Since dive profiles can be classified both by their type and by the degree of risk they pose, meaningful extrapolations include those between profiles of the same type but with different degrees of risk and those between profiles that differ both by type and by the degree of risk they pose.

There is of course a trade-off involved here. By restricting the calibration dataset to profiles of a particular kind, one necessarily reduces the size of the dataset from what it might otherwise be. This usually has the effect of reducing the accuracy of the fitted parameters. For the parallel models, it also resulted here in an inability to distinguish the 3CP model from the 2CP model. However, as explained below, neither of these drawbacks resulted in a major sacrifice.

Specifically, it will be shown that two other 3CP models, "USN93" (Ref. 35 and references therein), and "EE1(nt)" (34), which are very similar to the 3CP model initially considered here, but were calibrated using large, mixed-profile datasets, produced extrapolations that were qualitatively similar to those of the 2CP model (see Fig. 2 and Table 3). The 2CP model was calibrated using the purely square-profile dataset described below. Consequently, the inability to include our own particular form of the 3CP model in this study was relatively unimportant.

Furthermore, as shown by the entries in Table 2, each of the compartmental rate constants (the k_i s and λ_i s) for each of the five models studied were well resolved. Specifically, each rate constant in a given model was distinct from all other rate constants in that model at the 95% level of confidence. This level of confidence is the commonly accepted standard in the field and is sufficient for the present purpose. Any reduced accuracy of the parameters due to the limited size of the calibration dataset used was also, therefore, relatively unimportant.

The limitations inherent in the reduced size of the calibration dataset were therefore knowingly accepted, in exchange for the means to assess the quality of a model's extrapolations. In view of the purpose of this work, the benefit was judged to outweigh the cost.

The calibration dataset consisted of 725 square profile dives using air, for which the overall average *P*(DCS) was ~0.11. It is described in greater detail below and in Table 1. Two sets of points (the "target sets") were used to check the quality of the extrapolations. *1*) One set of points consists of points generated by the Hill multi-species model in the very high-risk square profile saturation regime (24). Three points in this regime are shown in Fig. 2 .The *P*(DCS) values for this set of points range from ~0.34 to 0.90. *2*) The other is the dataset that was used to validate the DSAT Recreational Dive Planner (10). The

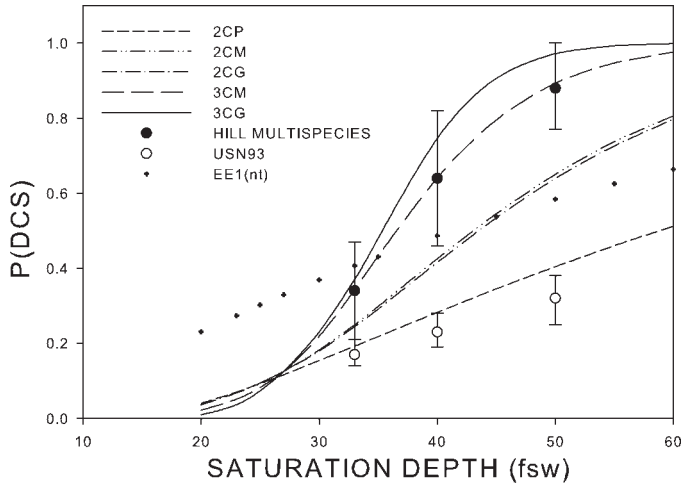

Fig. 2. Probability of developing DCS [*P*(DCS)] projections of the five models in the high-risk saturation regime [i.e., beyond 33 feet of seawater (fsw)] for direct-ascent saturation profiles. Predictions from the Hill multi-species model and the USN93 model, both taken from Ref. 24, are included for comparison, as are those of the EE1(nt) model (34). The error bars on the points are 95% binomial confidence intervals.

Table 1. *Sources of calibration data (33)*

Type of Dive	Dataset Name	Profiles Used
Saturation, air, ≥1,440 min	ASATDC	1–15
	ASATFR85	1–3
	ASATNMR	1–34
	ASATNSM	1–13
	EDUAS45	1, 12–15
	NMR9209	1–15
Subsaturation, air, 360–720 min	EDU84952	1–35
	NSM6HR	1–19
	RNPLX50	1–5, 7–16
Short duration, air, 5–205 min	DC4D	228, 237
	EDU849LT2	1–74
	EDU885A	37, 40, 41
	NMRNSW2	1–28

There were 180, 173, and 372 separate dives (also called man-dives) in the saturation, subsaturation, and short-duration categories, respectively. These incurred 17, 20, and 33 decompression sickness (DCS) cases, and 13, 19, and 49 marginal cases, respectively.

underlying profiles here involve a mix of different profile types. They include square, multilevel, repetitive, and short-duration dives, all on air, for which the overall average P(DCS) was of the order of 0.001. Additional details are given in Table 3.

Thus two different extrapolations are possible. With *target 1*, the extrapolation is from square profiles of low to high risk, to square profiles of very high risk. With *target 2*, the extrapolation is from square profiles of low to high risk, to a mix of extremely low-risk profiles of different types.

The parameter estimates for all five models were obtained by a calibration to the dataset described in Table 1. The data were used considering only the total DCS incidence rates, without regard to the time of onset of DCS (34, 35). It has been suggested (4, 35) that time of onset data may be sensitive to kinetic processes (such as biological processes induced by bubble formation and/or growth) that are beyond the scope of this work. With this choice, the dataset consisted of 82 square profiles (direct ascent and descent) distributed over 725 dives, with 180 saturation dives (≥1,440 min), 173 subsaturation dives (360–720 min) and 372 short-duration dives (5–205 min). "Marginals" (i.e., mild DCS-like cases that resolve themselves without recompression therapy) were weighted as 0.1 hits, mostly because this was the weight used for the calibration of the USN93D model, against which comparisons are made (Table 4).

Maximum likelihood (3, 36, 40) was the statistical basis used to fit the models to the data. The details on how the method was implemented here and how the reported confidence intervals were determined are given in APPENDIX B, *sections 2* and *3*.

P(DCS) calculations. The calculation of model-predicted P(DCS) values, both for the calibrations and applications, starts with the calculation of the risk function $r_i(t)$, defined in *Eq. 1*. As described in APPENDIX B, the time integral of $r_i(t)$ over the decompression phases of the dive profile provides the integrated risk, which is directly related to P(DCS). As shown in *Eq. 1*, $r_i(t)$ requires $p_i(t)$ in the risk-bearing compartment(s) of the model at any arbitrary point on the dive profile. The $p_i(t)$ expressions for the independent, parallel, perfusion-limited model (Fig. 1*A*) are obtained by a straightforward integration of the underlying first-order independent rate equations (one for each compartment) for each segment of the dive profile. They have been given elsewhere (Refs. 34, 36 and references therein). The way these expressions were implemented here is described in APPENDIX B, *section 1b*.

The general $p_i(t)$ expressions for the interconnected models have not previously been derived. They are obtained by analytical integration of the underlying coupled rate equations (APPENDIX A and *Eq. A2*). The general form of the result is given by *Eq. A3*, and its working form for this application is given by *Eq. A10*. The way this equation is used to obtain P(DCS) values for the interconnected models at arbitrary points on a dive profile is outlined in APPENDIX B, *section 1a*.

Statistical functions. A modern version of χ^2 testing, based on evaluating the incomplete gamma function (P) was used. The functions ν and Q represent the number of degrees of freedom and the complement of P [i.e., $(1 - P)$], respectively. The relationship between these quantities is shown in *Eq. 2* (30).

$$Q = \frac{\int_{\chi^2/2}^{\infty} e^{-x} x^{\frac{\nu-2}{2}} dx}{\int_{0}^{\infty} e^{-x} x^{\frac{\nu-2}{2}} dx} \qquad (2)$$

Q is a very useful statistical function. It represents the probability or, equivalently, the "level of confidence" at which a model can be taken to be consistent with the dataset against which it is being compared (30). The advantage of using Q, as opposed to traditional χ^2 look-up tables, is that, unlike the latter, the former provides the result of a consistency check as a definite value. For example, with look-up tables, the result of a consistency check might take the form "the model is consistent with the dataset at the 95% confidence level but not at the 99% confidence level." Using Q, the result of the same consistency check would take the form "the model is consistent with the dataset at the 96.2% confidence level." The widespread availability of low-cost, high-speed computing has rendered the calculation of Q by *Eq. 2* trivial. Look-up tables were constructed to avoid having to calculate Q (from χ^2 and ν) at a time when this calculation was nontrivial.

RESULTS

Six models were initially considered and fitted to the dataset in Table 1. They consisted of two perfusion-limited, independent, parallel compartment models (2CP and 3CP) and four interconnected models (2CM, 2CG, 3CM, and 3CG). It was found that the three-compartment independent parallel model (3CP) provided a fit to this dataset that was statistically indistinguishable from that provided by the 2CP model. In other words, this dataset could not be used to resolve the six independent parameters of the 3CP model. Consequently, the 3CP model as constituted here was not considered further. Also, for reasons unrelated to the calibration dataset used, it was not possible to resolve more than two f_{ij}s and three f_{ij}s for the interconnected two-compartment and three-compartment models, respectively (see APPENDIX A). Consequently, the fast rate constants (f_{10}, f_{12} for the 2CM and 2CG models and f_{10}, f_{12}, f_{13} for the 3CM and 3CG models) were approximated by their respective average values. These average values are represented in Table 2 by the symbol f_{1x}.

The λ_i s in Table 2, the model eigenvalues, have important physical significance. Their magnitudes are the characteristic compartmental decay constants for the interconnected models. There are two λ_i s (λ_1, λ_2) per compartment for the two-compartment interconnected models and three λ_i s (λ_1, λ_2, λ_3) per compartment for the three-compartment interconnected models. The λ_i s are functions only of the f_{ij} s. The relations that connect the λ_i s to the f_{ij} s are given by *Eqs. A4* and *A12* in APPENDIX A.

ν is here given by the number of profiles (82) less the number of fitted parameters (three or four, depending on the model). χ^2 for each model was determined from $2\ln[L(\text{perfect})/L(\text{actual})]$ where L(perfect) and L(actual) are the likelihood

Table 2. *Fitted values of the model parameters, decay constants, eigenvalues, 95% confidence intervals, and goodness-of-fit functions for the 5 models studied*

	Model				
Constant, min^{-1}	2CP	2CM	2CG	3CM	3CG
$k_1 \times 10^2$	0.151 (0.020–0.62)				
$k_2 \times 10$	0.112 (0.020–0.31)				
$c_1 \times 10^2$	0.120 (0.047–0.49)				
$c_2 \times 10^2$	0.427 (0.23–0.62)				
$f_{1x} \times 10$		0.140 (0.058–0.22)	0.133 (0.077–0.29)	1.00 (0.18–3.0)	4.47 (1.4–252)
$f_{21} \times 10^2$		0.322 (0.15–0.68)	0.223 (0.12–0.46)	7.94 (3.3–45)	4.81 (2.8–10)
$f_{31} \times 10^2$				0.319 (0.22–0.51)	0.177 (0.13–0.24)
$c \times 10$		0.123 (0.085–0.22)	0.121 (0.073–0.27)	0.376 (0.11–0.68)	0.836 (0.40–1.3)
$-\lambda_1 \times 10$		0.296 (0.12–0.45)	0.278 (0.13–0.41)	3.33 (0.78–9.3)	13.6 (4.3–757)
$-\lambda_2 \times 10$		0.0152 (0.007–0.030)	0.0150 (0.008–0.029)	0.487 (0.20–1.5)	0.414 (0.19–0.66)
$-\lambda_3 \times 10^2$				0.157 (0.10–0.20)	0.130 (0.098–0.24)
Statistical Functions					
ν	78	79	79	78	78
χ^2	76.2	67.7	67.7	66.7	55.2
Q	0.537	0.813	0.813	0.815	0.977

For the two-compartment mammillary (2CM) and two-compartment general (2CG) models, f_{20} is 0 and $0.2f_{21}$, respectively. For the three-compartment mammillary (3CM) model, f_{20} and f_{30} are both 0. For the three-compartment general (3CG) model, $f_{20} = 0.2f_{21}$, and $f_{30} = 0.2f_{31}$ (further details in APPENDIX A). 2CP, two-compartment parallel.

functions for the theoretically best possible (or "perfect") model and the actual model, respectively (3, 40). Q was determined from *Eq. 2*.

As seen from the entries in Table 2, Q is highest for the 3CG model, is lower for the 2CM, 2CG, and 3CM models, all of which have similar values for Q, and is lowest for the 2CP model. Therefore, the 3CG model represents the dataset best, followed by the 2CM, 2CG, and 3CM models (which are equivalent in this respect), followed by the 2CP model.

The fairly broad confidence intervals entered for some of the rate constants in Table 2 are, in part, a consequence of the limited dataset that was used for the calibrations. Nevertheless, as mentioned previously, each of the compartmental rate constants for each of the five models listed in Table 2, were resolved at the 95% level of confidence.

The plots in Fig. 2 show the *P*(DCS) predictions of the five models when extrapolated to the very high-risk saturation regime. The calibration dataset contained saturation profiles up to and including 33 fsw depth, so those portions of the plots to the right of 33 fsw are extrapolations. These extrapolations serve as a basic test of the robustness of the five models, assessing their accuracy as risk levels increase while the profile type remains unchanged.

The Hill multi-species model is the best available basis for checking these extrapolations. It is based on combining human air saturation data with high-risk, scaled, pig and rat air saturation data (24). The mixing of the scaled, high-risk animal data with the human data is believed to have produced a more reliable predictive curve in the very high-risk saturation regime than can be obtained from human saturation data alone (24). It is seen that both the 3CM and 3CG models are in agreement with the Hill multi-species predictions at depths of 40 and 50 fsw, whereas the 2CM, 2CG, and 2CP models are not. These models' predictions are too low. Also, it is clear that the curves for the 3CM and 3CG models each have the correct shape, whereas those for all the other models shown do not. The 2CP model's curve has the same (incorrect) shape as those of the USN93 and EE1(nt) models, which are included in Fig. 2 for comparison. These are 3CP models that were calibrated elsewhere using large mixed-profile datasets. The points shown for the USN93 model were taken from Ref. 24; those for the EE1(nt) model were calculated in this work using the parameters reported for this model in Ref. 34.

It is significant that all four interconnected models predict higher extrapolated *P*(DCS) values than does the 2CP model. This can be interpreted as being due to the peripheral compartment(s) in the interconnected models acting as inert gas sources, feeding dissolved nitrogen to the central risk-bearing compartment during decompression from saturation. By transferring excess nitrogen from the non-risk-bearing compartment(s) to the risk-bearing compartment, they raise the predicted risk for these profiles relative to what it would be in the absence of this mechanism.

The results of extrapolating the five models to a very different regime are given in Table 3. The datasets listed there are for short-duration, very low-risk dives on air. They include mostly multilevel profiles, many done as repetitive dives. These profiles are somewhat representative of recreational diving (10). There was only one incidence of DCS (in one of the *phase 2A* dives) in the entire dataset of 1,437 single dives or 565 dive sets. (A dive set is a group of one or more dives, followed by at least an 8-h surface interval.) The function Q, introduced previously, is again used as a measure of the level of consistency of the model's predictions with the observed data. Here, however, the number of degrees of freedom (ν) is given simply by the number of profiles, since these datasets were not used to calibrate the models.

This is a very demanding test of model robustness, since the extrapolation is to a regime characterized by both a much lower level of risk and profiles of a different type from those in the calibration dataset. In view of this, it is seen that the 3CG model performs remarkably well, the 3CM model's performance is fair, whereas the 2CP, 2CM, 2CG, and EE1(nt) models all perform poorly. As indicated previously, the EE1(nt) model is a 3CP model that was calibrated elsewhere

Table 3. *Probability of consistency Q of 6 models with datasets relevant to recreational diving.*

Dataset (Ref. 10)	No. of Single Dives	No. of Dive Sets	No. of Dive Profiles (ν)	Q (χ^2)					
				EE1(nt)	2CP	2CM	2CG	3CM	3CG
Phase 1	911	437	25	$0–10^{-6}$ (207)	0.35×10^{-3} (56.1)	0.95 (14.5)	0.97 (13.8)	0.36 (26.7)	0.98 (12.6)
Phase 1+ 2B	1386	557	31	$0–10^{-6}$ (278)	0.50×10^{-4} (71.4)	0.92 (20.7)	0.93 (20.2)	0.24 (36.2)	0.93 (20.2)
Phase 1 + 2A + 2B	1437	565	33	$0–10^{-6}$ (280)	0.71×10^{-4} (73.2)	0.0 (∞)	0.0 (∞)	0.25 (38.0)	0.93 (21.9)

Entries in parentheses are the underlying χ^2 values, and the number of degrees of freedom (ν) is here equal to the number of dive profiles. The entries for the EE1(nt) model were determined in this work using the parameter values for this model reported in Ref. 34. The numerical algorithm used to determine Q loses accuracy when χ^2 is very large. Consequently, an estimated range for Q is shown for the EE1(nt) model.

using a large mixed-profile dataset. The very low values of Q for both the 2CP and EE1(nt) models stem from these models' significant overestimation of P(DCS) for these profiles. Specifically, the P(DCS) predictions from the 2CP and EE1(nt) models for the entire dataset (*phase 1 + 2A + 2B*) were distributed around ≈0.06 and ≈0.22, respectively. In contrast, the corresponding 3CM and 3CG models' predictions were distributed around ≈0.03 and ≈0.01, respectively. The empirical P(DCS) confidence intervals for the entire dataset can be rigorously calculated only if it is assumed that all the dive sets in the dataset had the same profile (3, 10). Under this assumption, the empirical 95% binomial confidence interval (for 1 incident in 565 identical dive sets) is 0–0.01. This can be taken as a rough estimate of the actual P(DCS) confidence interval for the entire dataset.

The 2CM and 2CG models performed erratically, with high, seemingly good Q values for the *phase 1* and *phase (1 + 2B)* datasets, but values of zero for the *phase (1 + 2A + 2B)* dataset. The latter stem from these models' P(DCS) predictions of exactly 0.0 for the one dive set (in *phase 2A*) that actually produced a hit. This causes χ^2 to become infinite and Q to become zero (see *Eq. 2*).

The entries in Table 4 can be used to compare the level of agreement of the P(DCS) predictions of the five models with those of the USN93D model for 17 well known square profiles. These are the USN "NDLs"; i.e., the allowed no-decompression bottom times for square profiles with depths in the range of 35–190 fsw, using air. Although no existing model can be considered a "gold standard," comparisons against the USN93D model with respect to these profiles are informative. The USN93D model was calibrated against a larger dataset than was used here. This dataset consisted of 3,322 air and N_2-O_2 man-dives and involved a mix of profile types. Also, the predictions of the USN93D model for the USN NDLs were found to be highly consistent with those of a different model, the BVM(3) model (35). The high level of agreement between the USN93D and the BVM(3) models, with respect to these 17 square profiles, lends partial support to each of their sets of predictions.

The 3CM and 3CG model results are in fairly good agreement with the USN93D P(DCS) predictions, considering the much more limited calibration dataset used here. For each of these models, 15 of 17 P(DCS) predictions are in accord with the corresponding USN93D values, in the sense that the correspond-

Table 4. *Comparison of the P(DCS) predictions (%) of the 5 models against those of the USN93D model for the 17 USN NDL's (37)*

Depth, fsw	Bottom Time, min	Model					
		USN93D	2CP	2CM	2CG	3CM	3CG
35	310	5.5 (4.5–6.7)	8.6 (4.0–13)	5.1 (3.1–6.8)	5.3 (3.6–7.0)	3.2 (1.8–5.0)	1.5 (0–2.7)
40	200	4.0 (3.2–5.0)	9.5 (2.9–13)	4.9 (3.0–6.4)	5.1 (3.9–7.2)	3.1 (1.8–4.5)	1.5 (0–2.8)
50	100	2.5 (2.0–3.3)	8.3 (3.4–10)	5.1 (3.4–6.3)	5.3 (3.6–6.6)	3.5 (1.9–4.7)	1.9 (.06–3.4)
60	60	2.1 (1.6–2.8)	6.0 (3.4–8.0)	4.8 (1.8–6.0)	4.9 (2.0–6.2)	4.2 (2.1–5.1)	2.3 (.2–4.0)
70	50	2.4 (1.8–3.1)	6.3 (3.7–8.6)	5.8 (2.2–7.4)	5.8 (2.4–7.4)	5.5 (2.8–6.8)	3.5 (1.0–5.3)
80	40	2.4 (1.8–3.1)	5.8 (3.0–8.5)	5.9 (1.6–8.0)	5.9 (1.7–7.9)	6.4 (3.2–8.4)	4.1 (1.4–6.3)
90	30	2.1 (1.6–2.8)	4.2 (1.4–7.1)	4.9 (.3–7.4)	4.8 (.3–7.2)	6.6 (2.9–9.3)	3.6 (.9–6.5)
100	25	2.1 (1.5–2.8)	3.6 (.9–6.5)	4.6 (0–7.3)	4.4 (.1–6.9)	7.0 (2.5–10)	3.6 (.8–6.7)
110	20	1.9 (1.4–2.6)	2.6 (.3–5.3)	3.7 (0–6.3)	3.5 (0–5.7)	6.9 (1.7–11)	3.0 (.3–6.7)
120	15	1.7 (1.1–2.3)	1.3 (0–3.8)	2.2 (0–4.6)	2.0 (0–3.9)	6.2 (0.6–10)	2.1 (0–5.3)
130	10	1.3 (0.8–2.1)	0.1 (0–2.1)	0.5 (0–2.1)	0.4 (0–1.7)	4.8 (0–8.5)	1.2 (0–3.5)
140	10	1.5 (0.9–2.2)	0.3 (0–2.6)	0.8 (0–2.7)	0.7 (0–2.2)	5.5 (0.04–9.6)	1.4 (0–4.0)
150	5	1.1 (0.6–1.9)	0 (0–0.4)	0 (0–0.1)	0 (0–0.01)	2.7 (0–4.9)	0.5 (0–2.3)
160	5	1.2 (0.6–2.0)	0 (0–0.5)	0 (0–0.2)	0 (0–0.07)	3.0 (0–5.5)	0.6 (0–2.5)
170	5	1.2 (0.7–2.1)	0 (0–0.7)	0 (0–0.3)	0 (0–0.2)	3.4 (0–6.1)	0.7 (0–2.8)
180	5	1.3 (0.7–2.2)	0 (0–0.8)	0 (0–0.5)	0 (0–0.3)	3.8 (0–6.7)	0.8 (0–3.0)
190	5	1.3 (0.8–2.2)	0 (0–1.0)	0 (0–0.7)	0 (0–0.5)	4.1 (0–7.3)	0.8 (0–3.2)
Mean		2.1	3.3	2.8	2.8	4.7	1.9

The entries in parentheses are 95% confidence interval estimates, and the entries for USN93D are from Ref. 35. P(DCS), probability of developing DCS; fsw, feet of seawater.

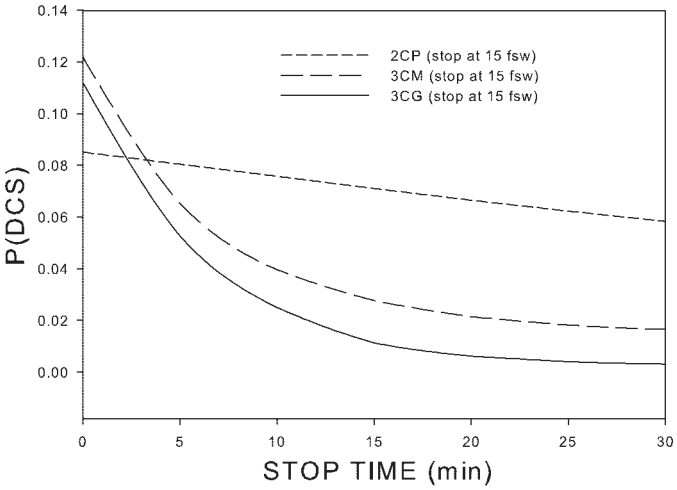

Fig. 3. The effect of stop time on P(DCS) for a dive to 120 fsw for 30 min, according to the two-compartment, independent, parallel (2CP), three-compartment mammillary (3CM), and three-compartment general (3CG) models.

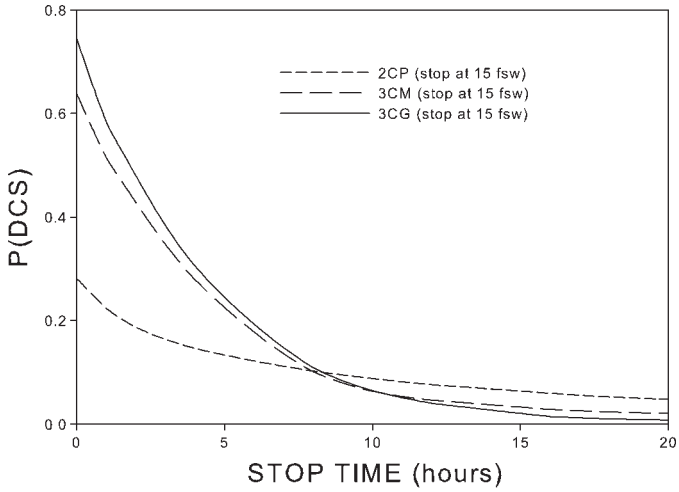

Fig. 5. The effect of stop time on P(DCS) for a dive to 40 fsw for 24 h, according to the 2CP, 3CM, and 3CG models.

ing 95% confidence intervals overlap. The level of agreement is not as good for the 2CP, 2CM, and 2CG models where only 12, 11, and 12, respectively, of the 17 P(DCS) predictions are in accord with the corresponding USN93D values.

The results shown in Fig. 2 and Tables 3 and 4 are indicative of a clear division in performance and reliability between the 2 two-compartment and the 2 three-compartment interconnected models. The 3CM and 3CG models extrapolate beyond the calibration regime and interpolate within it more accurately than do the 2CM and 2CG models. This suggests that three-exponential (as opposed to two-exponential) compartmental kinetics are needed to adequately handle these applications. For this reason, the 2CM and 2CG models will not be considered further. The remaining results, which are shown in Figs. 3–5, involve comparisons of the 2CP, 3CM, and 3CG models in applications for which the interconnected and parallel models differ significantly with respect to their predictions. Empirical P(DCS) values and/or gas washout data for these profiles do not exist; the quantitatively "correct" behavior is, therefore, unknown. The main purpose of showing these results is to illustrate the properties of the 2CP, 3CM, and 3CG models and to account for their different predictions in terms of their basic kinetic properties. Both the descent and ascent rates in these applications were 60 fsw/min.

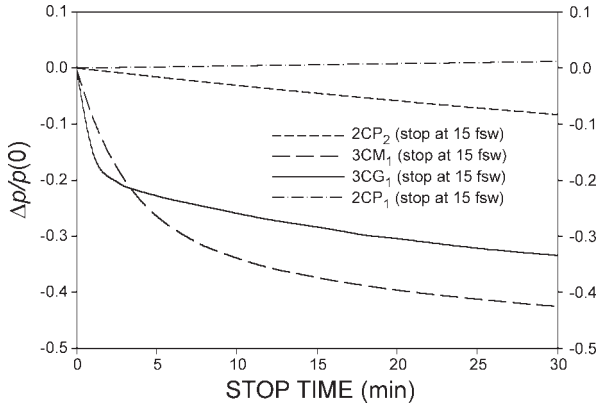

Fig. 4. The fractional change in the Henry's law-based N_2 partial pressure $p(t)$ for the dive in Fig. 3 as a function of stop time t. $\Delta p = p(t) - p(0)$, where $p(0)$ represents $p(t)$ at the start of the decompression stop in the indicated compartment (written as a subscript). The $p(0)$ values (in atm) were 0.868 ($2CP_1$), 1.55 ($2CP_2$), 1.87 ($3CM_1$), and 1.63 ($3CG_1$).

Figure 3 displays the degree of risk-abatement, as predicted by each of these models, as a function of decompression stop time for a stop at 15 fsw. The dive is of short duration (120 fsw, 30 min) and is in the moderate-risk regime [model-predicted P(DCS) ≈ 0.10 when it is done as a direct ascent]. It is seen that both interconnected models predict a much steeper initial drop in P(DCS) with increasing stop time than that predicted by the parallel model. Also, the magnitude of the slopes of the curves for the interconnected models decreases rapidly with increasing stop time to the extent that, by 30 min, these curves are almost flat. This indicates that lengthening the stop time beyond 30 min would provide no additional benefit. In contrast, the rate of P(DCS) abatement predicted by the 2CP model is much more uniform, being slower for $t < 10$ min and faster at $t \approx 30$ min, than that of the interconnected models. Figure 3 shows that, according to the 2CP model, lengthening the stop time beyond 30 min would provide (considerable) additional benefit.

These differences are a consequence of the different washout functions of interconnected and independent compartmental models. At a fixed depth, the washout function for (the risk-bearing) *compartment 1* in the interconnected models can be written as (see *Eq. A10*):

$$\frac{dp_1(t)}{dt} = \sum_{j=1}^{3} \alpha_j \lambda_j e^{\lambda_j t} \qquad (3)$$

where $\alpha_j = c_j + [k_j(0)/\lambda_j]$. The constants c_j, $k_j(0)$, and, therefore, α_j are model- and profile-dependent. "Profile-dependent" here means that the numerical values of these constants depend on the details of the depth vs. time profile that was executed from the start of the dive to the start of the decompression stop being considered. They are "constants" in the sense that they are invariant with t, the time spent at the decompression stop (see APPENDIX A). The eigenvalues (λ_1, λ_2,

λ_3), whose magnitudes represent the compartmental decay constants, do not depend on profile or time. The values of α_1, α_2, and α_3 were +0.51, +0.38, and −0.12 and +0.31, +0.34, and −0.12 atm for the stop shown in Fig. 3 for the 3CM and 3CG models, respectively. From these values of α_j, and the λ_j values in Table 2, it is readily shown, using *Eq. 3*, that the j = 1 term, which represents the contribution to the sum by the most negative eigenvalue (λ_1), will be negative and will dominate $dp_1(t)/dt$ at short stop times ($t < 7$ min, 3CM; $t < 2$ min, 3CG). The j = 3 term, which represents the contribution of the least negative eigenvalue λ_3, will be positive and will dominate (the very small values of) $dp_1(t)/dt$ at asymptotically long times ($t > 120$ min, 3CM and 3CG). The j = 2 term dominates the sum at intermediate times and contributes negatively to it. As a result of all this, the initial washout rate from *compartment 1* will be relatively fast and will slow down considerably as the stop time increases.

For probabilistic models consisting of perfusion-limited, independent parallel compartments, the total DCS risk for a given profile is usually dominated by the contribution made to it by one of the model's compartments. For example, for the profile in Fig. 3, *compartment 2* makes a much larger contribution to *P*(DCS) than does *compartment 1*, so that, as a good approximation, $dp_2(t)/dt$ alone describes the washout that affects risk. At a fixed depth, $dp_2(t)/dt = \beta_2 k_2 e^{-k_2 t}$, where β_2 is profile- and model-dependent and k_2 is the rate constant for *compartment 2*. The function $\beta_2 k_2 e^{-k_2 t}$ changes much more slowly with time during the decompression stop than does the right-hand side of *Eq. 3*. This is readily confirmed by comparing the values of $d^2p_1(t)/dt^2$ with those of $d^2p_2(t)/dt^2$ for $0 \leq t \leq 30$ min. The value of β_2 is −0.452 atm for this stop, and k_2 (from Table 2) is 0.0112/min. The more uniform washout rate for the parallel model, relative to the interconnected models, results from having, to a good approximation, only one rate constant (k_2) and one term ($\beta_2 k_2 e^{-k_2 t}$) in the relevant washout rate expression, as opposed to three.

A consequence of these different washout rate functions is illustrated in Fig. 4. This figure shows the size of the fractional change of the Henry's law-based nitrogen partial pressure in the risk-bearing compartments as a function of stop time during the decompression stop for the dive in Fig. 3 for each of the models. The fractional drop in the nitrogen partial pressure over the stop times shown is clearly much larger for the 3CM and 3CG models than for the 2CP model. This accounts for the different risk-abatement patterns shown in Fig. 3. Because of the more extensive off-gassing of the risk-bearing compartments of the 3CM and 3CG models during a short stop, these models predict a significantly reduced degree of supersaturation in these compartments on surfacing after the stop relative to predictions of the 2CP model. Since the DCS risk after surfacing from the dive makes the dominant contribution to the total risk for these profiles, one gets larger *P*(DCS) abatements from short stops with the interconnected models than with the independent parallel compartmental model.

A comparison of Figs. 3 and 4 illustrates an important distinction in the amount of information contained by the functions *P*(DCS) and $p_1(t)$. The latter contains more information than the former. For example, the crossover of the $3CM_1$ and $3CG_1$ curves at ~4 min, shown in Fig. 4, is lost in the *P*(DCS) curves shown for these models in Fig. 3. As discussed in APPENDIX A, the loss of information that results from the use of *P*(DCS) data for model calibration, as opposed to washout data [i.e., $p_1(t)$ vs. t], severely limits the theoretical maximum number of resolvable rate constants for the interconnected models. This theoretical maximum (for a given interconnected model) is independent of the size or composition of the dataset used for model calibration (see APPENDIX A).

Figure 5 demonstrates the generality of the result illustrated in Fig. 3. Here, *P*(DCS) vs. stop time, as predicted by each of these models, is shown for a very high-risk saturation dive (40 fsw, 24 h). Although the time scale, as expected, is now in hours rather than minutes, the risk-abatement patterns in Fig. 5 are seen to be similar to those in Fig. 3. The relatively more rapid initial risk-abatement predicted by the interconnected models is seen to recur when the profile is changed from a moderate-risk bounce dive to a very high-risk saturation dive.

DISCUSSION

Of the two 2-compartment (2CM, 2CG) and two 3-compartment (3CM, 3CG) interconnected models studied, the 3CM and 3CG models were more accurate. The 3CM and 3CG models provided a better fit to the calibration dataset, interpolated better within the risk regime represented by it, and extrapolated more accurately outside of the calibration regime, than did the 2CP independent parallel compartment model. The 2CP, 3CM, and 3CG models were all based on linear kinetics, made use of exactly the same probabilistic risk function, were calibrated using the identical dataset, and had the same number of fitted parameters.

The different *P*(DCS) predictions from the parallel and interconnected models can be understood from their fundamentally different washout characteristics. The correct shape of the curves shown in Fig. 2 for the 3CM and 3CG models is a consequence of their peripheral compartments providing dissolved nitrogen to the central compartment during decompression from saturation. The key factor that accounts for the different risk-abatement patterns shown in Figs. 3 and 5 is the greater initial washout rate from the central compartment of the interconnected models during the decompression stop.

If the above predictions are empirically confirmed, the practical implications for diving could be significant.

ACKNOWLEDGMENTS

The author thanks Peter Tikuisis for reprints, DSAT for copies of their publications on the testing programs that underlie the Recreational Dive Planner, and Ethel Goldman, both for useful comments and for helping to prepare this manuscript for publication. The author is also very grateful to three reviewers, whose detailed comments, references, and constructive criticism helped to significantly improve this article.

REFERENCES

1. **Avni Y.** Energy spectra of X-ray clusters of galaxies. *Astrophys J* 210: 642–646, 1976.
2. **Boycott AE, Damant GCC, Haldane JA.** Prevention of compressed air illness. *J Hyg London* 8: 342–443, 1908.
3. **Brownlee KA.** *Statistical Theory and Methodology in Science and Engineering* (2nd ed.). New York: Wiley, 1965.
4. **Doolette DJ, Mitchell SJ.** Biophysical basis of inner ear decompression sickness. *J Appl Physiol* 94: 2145–2150, 2003.
5. **Doolette DJ, Upton RN, Grant C.** Countercurrent compartmental models describe hind limb skeletal muscle helium kinetics at resting and low blood flow in sheep. *Acta Physiol Scand* 185: 109–121, 2005.

6. **Doolette DJ, Upton RN, Grant C.** Perfusion-diffusion compartmental models describe cerebral helium kinetics at high and low cerebral blood flows in sheep. *J Physiol* 563: 529–539, 2005.
7. **Doolette DJ, Upton RN, Grant C.** Diffusion-limited, but not perfusion-limited compartmental models describe cerebral nitrous oxide kinetics at high and low blood flows. *J Pharmacokinet Biopharm* 26: 649–672, 1998.
8. **Geman S, Geman D.** Stochastic relaxation, Gibbs distributions, and the Bayesian restoration of images. *IEEE Trans Pattern Anal Machine Intel* 6: 721–741, 1984.
9. **Goldberg JL, Schwartz AJ.** *Systems of Ordinary Differential Equations: An Introduction*. New York: Harper and Row, 1972.
10. **Hamilton RW, Rogers RE, Powell MR, Vann RD.** *Development and Validation of No-Stop Decompression Procedures for Recreational Diving: The DSAT Recreational Dive Planner*. Uniontown, OH: DSAT and Hamilton Research, 1994.
11. **Hildebrand JH, Scott RL.** *The Solubility of Non Electrolytes*. New York: Dover, 1964, p. 18.
12. **Hills BA.** *Decompression Sickness* (Vol. 1). New York: Wiley, 1977, p. 44, 45, 58–60.
13. **Hills BA.** The variation in susceptibility to decompression sickness. *Int J Biometeorol* 12: 343–349, 1968.
14. **Hochstadt H.** *Differential Equations: A Modern Approach*. New York: Holt, Rinehart & Winston, 1964.
15. **Homer LD, Weathersby PK, Survanshi S.** How countercurrent blood flow and uneven perfusion affect the motion of inert gas. *J Appl Physiol* 69: 162–170, 1990.
16. **Jacquez JA.** *Compartmental Analysis in Biology and Medicine* (2nd ed.). Ann Arbor, MI: The Univ. of Michigan Press, 1985.
17. **Ketty SS.** The theory and applications of the exchange of inert gas at the lungs and tissues. *Pharmacol Rev* 3: 1–41, 1951.
18. **Kidd D, Stubbs RA, Weaver RS.** Comparative approaches to prophylactic decompression. In: *Proceedings of the 4th Symposium on Underwater Physiology*, edited by Lambertsen CJ. New York: Academic, 1971. p. 167–177.
19. **Kirkpatrick S.** Optimization by simulated annealing: quantitative studies. *J Stat Phys* 34: 975–986, 1984.
20. **Kirkpatrick S, Gelatt CD Jr, Vecchi MP.** Optimization by simulated annealing. *Science* 220: 671–680, 1983.
21. **Klotz IM.** *Chemical Thermodynamics*. New York: Benjamin, 1964. p. 336–355.
22. **Knuth DE.** *The Art of Computer Programming. Semi Numerical Algorithms* (2nd ed.). Reading, MA: Addison-Wesley, 1981, vol. 2, p. 120.
23. **Lampton M, Margon B, Bowyer S.** Parameter estimation in X-ray astronomy. *Astrophys J* 208: 177–190, 1976.
24. **Lillo RS, Himm JF, Weathersby PK, Temple DJ, Gault KA, Dromsky DM.** Using animal data to improve prediction of human decompression risk following air-saturation dives. *J Appl Physiol* 93: 216–226, 2002.
25. **Morales MF, Smith RE.** On the theory of blood-tissue exchanges: III. Circulation and inert gas exchange at the lung with special reference to saturation. *Bull Math Biophys* 6: 141–152, 1944.
26. **Morales MF, Smith RE.** A note on the physiological arrangemnent of tissues. *Bull Math Biophys* 7: 47–51, 1945.
27. **Morales MF, Smith RE.** On the theory of blood-tissue exchange of inert gases: VI. Validity of approximate uptake expressions. *Bull Math Biophys* 10: 191–200, 1948.
28. **Nishi RY, Lauckner GR.** *Development of the DCIEM Decompression Model for Compressed Air Diving*. Downsview, Ontario, Canada: Defence and Civil Institute of Environmental Medicine, 1984, no. 84-R-44.
29. **Novotny JA, Mayers DL, Parsons YFJ, Survanshi SS, Weathersby PK, Homer LD.** Xenon kinetics in muscle are not explained by a model of parallel perfusion-limited compartments. *J Appl Physiol* 68: 876–890, 1990.
30. **Press WH, Flannery BP, Teukolsky SA, Vetterling W.** *Numerical Recipes. The Art of Scientific Computing (FORTRAN Version).* Cambridge, UK: Cambridge Univ. Press, 1989.
31. **Smith RE, Morales MF.** On the theory of blood-tissue exchanges: I. Fundamental equations. *Bull Math Biophys* 6: 125–131, 1944.
32. **Smith RE, Morales MF.** On the theory of blood-tissue exchanges: II. Applications. *Bull Math Biophys* 6: 133–139, 1944.
33. **Temple DJ, Ball R, Weathersby PK, Parker EC, Survanshi SS.** *The Dive Profiles and Manifestations of Decompression Sickness Cases after Air and Nitrogen-Oxygen Dives*. Bethesda, MD: Naval Medical Research Center, 1999. (NMRC Rep. 99-02)
34. **Thalmann ED, Parker EC, Survanshi SS, Weathersby PK.** Improved probabilistic decompression model risk predictions using linear-exponential kinetics. *Undersea Hyperb Med* 24: 255–274, 1997.
35. **Tikuisis P, Gerth WA.** Decompression theory. In: *Physiology and Medicine of Diving* (5th ed), edited by Elliott D and Bennett P. London: Saunders, 2003. p. 419–454.
36. **Tikuisis P, Nishi RY, Weathersby PK.** Use of the maximum likelihood method in the analysis of chamber air dives. *Undersea Biomed Res* 15: 301–313, 1988.
37. **US Department of the Navy.** *US Navy Diving Manual. Naval Sea Systems Command. Publication 0910-LP-708-8000, Rev 4*. Washington, DC: Naval Sea Systems Command, 1999.
38. **Vann RD.** Mechanisms and risks of decompression. In: *Diving Medicine* (2nd ed.), edited by Bove AA and Davis JC. Philadelphia, PA: Saunders, 1990.
39. **Weathersby PK, Barnard EEP, Homer LD, Mendenhall KG.** Stochastic description of inert gas exchange. *J Appl Physiol* 47: 1263–1269, 1979.
40. **Weathersby PK, Homer LD, Flynn ET.** On the likelihood of decompression sickness. *J Appl Physiol* 57: 815–825, 1984.
41. **Weathersby PK, Mendenhall KG, Barnard EEP, Homer LD, Survanshi S, Vieras F.** Distribution of xenon gas exchange rates in dogs. *J Appl Physiol* 50: 1325–1336, 1981.
42. **Weathersby PK, Survanshi SS, Homer LD, Hart BL, Bradley ME.** Statistically based decompression tables. I. Analysis of standard air dives: 1950-1970. NMRI report 85-16. Bethesda, MD: Naval Medical Research Institute, 1985.
43. **Weathersby PK, Survanshi SS, Nishi RY.** Relative decompression risk of dry and wet chamber air dives. *Undersea Biomed Res* 17: 333–351, 1990.